Multimodal Spectral Focusing CARS and SFG Microscopy with a Tailored Coherent Continuum from a Microstructured Fiber

KRZYSZTOF P. HERDZIK,[1,2] **KONSTANTINOS N. BOURDAKOS,**[2] **PETER B. JOHNSON,**[2,3] **ADAM P. LISTER,**[2,3] **ALEKSANDRA P. PITERA,**[2] **CHUN-YU GUO,**[4] **PETER HORAK,**[1] **DAVID J. RICHARDSON,**[1] **JONATHAN H. V. PRICE,**[1]* **SUMEET MAHAJAN**[2,3]*

[1]*Optoelectronics Research Centre, University of Southampton, SO17 1BJ, UK*
[2]*Institute for Life Sciences, University of Southampton, SO17 1BJ, UK*
[3]*School of Chemistry, University of Southampton, SO17 1BJ, UK*
[4]*College of Electronic Science and Technology, Shenzhen University, China*
**jhvp@soton.ac.uk*
**s.mahajan@soton.ac.uk*

Abstract: We report a technologically novel microscopy system for bioimaging based on 100 fs Titanium:Sapphire (Ti:Sa) laser coherent continuum from a tailored, 9 cm long All Normal Dispersion (ANDi) fiber, enabling concurrent image contrast with a) Spectral Focusing Coherent Anti-Stokes Raman Scattering (SF-CARS) (spanning 900-3200 cm^{-1}) and b) sum-frequency-generation (SFG). Both modalities were efficiently excited with power levels at the microscope focus compatible with biological samples. Moreover, using the continuum, images were recorded in the back-scattering (epi-detection) geometry, without the necessity for an expensive, computer-controlled, Spatial Light Modulator (SLM), clearly demonstrating the strong signal levels achieved. Image contrast from the multiple modalities provided greater chemical and structural insights than imaging with any single technique in isolation. Numerical simulations supported these developments in regard to both the optimum fiber length for SC generation and the achievement of high spectral resolution in SF-CARS via careful group-delay-dispersion matching across the pump and Stokes pulses using just an inexpensive sequence of short glass blocks inserted into the Stokes beam. We show bio-images of mouse tissue recorded concurrently via label/stain-free contrast from multiple modalities: CARS, Two Photon auto-Fluorescence (TPaF) and Second Harmonic/Sum Frequency Generation (SHG/SFG). Overall our approach delivers optimum performance in back-scattered (epi-) detection configuration, suited for thick samples, at reduced complexity and cost. The addition of this simple fiber add-on to lasers already widely used for TPF microscopy can thus extend the capabilities of a significant number of existing microscopy laboratories.

1. Introduction

Coherent anti-Stokes Raman scattering (CARS) is an optical technique in which vibrational coherences are excited and probed to provide molecule selective detection. Spectroscopy and microscopy with CARS had been shown as early as 1965 [1] and 1982 [2], respectively. Due largely to the progress in laser technology over the last two decades CARS is emerging as a valuable imaging tool in biomedical research [3] as it provides label-free, non-destructive, non-invasive contrast, is relatively easy to implement and enables 3D imaging due to its inherent z-sectioning capability [4, 5]. CARS has provided important insights in neurology [6], cancer and tumor metastasis [7], embryonic and skeletal stem cells [8, 9], as well as in a range of in-vivo studies [10-12].

Briefly, CARS uses a shorter wavelength pump pulse, a longer wavelength Stokes pulse and, in 3-color CARS [12, 13], a further short wavelength pulse for the probe, together exciting anti-Stokes emission. Although technically a pump and Stokes are needed to excite the resonance from which a third ‘probe’ pulse creates the output, the pump beam is typically also used as a probe to avoid unnecessary complication. Tissue components that appear similar with white light microscopy can have very different Raman resonances thus enabling clear segregation of sub-structures. CARS entails the use of multiple excitation frequencies, which are currently generated either by using a tunable optical parametric oscillator-based system (OPO), or by using a broadband Stokes component generated by a supercontinuum (SC) fiber [14, 15]. However, the slow tuning speed of most current OPO systems, not to mention capital and maintenance costs, or the low spectral power density in SC-based broadband CARS, means that with these sources the acquisition of hyperspectral images can take hours [16]. Furthermore, despite the acknowledged benefits of CARS, the cost and size of the laser sources still limits its wider adoption. By matching the few-ps duration (~10 cm^{-1} bandwidth) of the molecular resonances observed in biological samples, the use of 2-10 ps pulses provide the optimum characteristics considering spectral resolution and maximal peak powers [17], which is why the most common implementation of CARS uses ps source lasers.

The majority of nonlinear laser biomicroscopy is based on Two Photon Fluorescence (TPF) [18] or Second Harmonic Generation (SHG) [19] to provide image contrast (signal). TPF is often carried out with natural (e.g. green fluorescent protein - GFP) fluorophores in genetically modified cells or transgenic organisms, or with exogenous artificial stains applied to the samples. Biological cells and tissues also have natural fluorophores, often with absorption in the UV-blue spectral region, so two-photon excited auto-fluorescence is feasible with NIR lasers. Second harmonic generation (SHG), a special case of sum frequency generation (SFG), allows imaging of non-centrosymmetric structures such as collagen in tissues in a label-free manner along with TPF. This is partly historical but mainly due to the simpler single-color, 100 fs, Ti:Sapphire (Ti:Sa) lasers available (Femtosecond (fs) sources have higher peak powers, which more efficiently excite these modalities). The result is a large installed base of fs Ti:Sa lasers and the ability to retrofit a CARS capability to such lasers could offer significant benefits by providing research teams working in the bio-imaging community with a label-free modality where the use of GFP or stains is not appropriate, and e.g. ultimately for diagnostics. Finally, we note that with CARS, epi-detection provides almost an order of magnitude weaker signals than forward detection, but is more versatile as it does not require sub-100 micron thick samples to be prepared [20-23], which is an important factor facilitating clinical impact.

A partly explored route towards meeting this challenge is continuum generation in microstructured optical fiber (MOF), output of which when chirped and cut into long- and short-wavelength pulses provides the pump and Stokes in so-called ‘spectral-focusing CARS’ (SF-CARS) [22]. Stretching the pulses linearly, means that a resolution similar to that for transform-limited ps pulses can be achieved [22, 24, 25]. In typical SF-CARS implementations, fs pulses have been stretched using dispersive glass elements [24, 26] and by equalizing the Group Delay Dispersion (GDD) between the pump and the Stokes by placing extra glass in the Stokes arm. The resolution of the system is dependent on the equalization of GDD which has been investigated analytically [25, 27]. The power requirements with SF-CARS are similar to single-frequency CARS, e.g. ~30 mW at the microscope focus is typically used with a high (>1) numerical aperture lens for bio-imaging due to photo-toxicity limitations.

Langbein *et al.* used the extreme bandwidth from a <10 fs Ti:Sa oscillator in a multimodal microscopy system targeting both the fingerprint region (1200-1800 cm^{-1}) and the high-wavenumber CH-stretch region (2800-3200cm^{-1}) [28] and later variations have used for example an offset probe to improve the signal to background ratio [29].

To avoid the need for a 10 fs oscillator for SF-CARS, methods using Stokes and pump carved from SC pulses generated in so-called microstructured fibers (MOFs) have been developed at significantly lower cost and are now widely used for SC pumped bioimaging [27, 30-32]. The SC in fibers such as the femtoWHITE 800 fiber from NKT is ordinarily generated in the anomalous dispersion regime, where the soliton fission threshold, above which the SC pulse breaks into multiple pulses, limits the coherence and reduces the effectiveness for exciting CARS signals [33]. To address this, the NL-1.4.775-945 NKT fiber was introduced commercially as an NKT femtoWHITE CARS module [34]. It has two closely spaced Zero Dispersion Wavelengths (ZDW) to avoid extended propagation in the anomalous dispersion regime thereby increasing the coherence. Such modules have been used for tissue imaging, spectroscopy [27] and CARS for resonances both in the fingerprint region and the CH-stretch region [31]. However, the excessive broadening due to the dispersive and nonlinear properties of the fiber limits the useful power available for CARS signal generation, so it has been applied only for CARS detected in the forward (transmission) direction, rather than in the weaker epi-direction (with one notable exception [35]), as would be needed for thick and hence easily prepared clinical samples [21-23].

Users of femtoWHITE CARS modules have, to-date, used a pick-off of the fs seed laser as the pump and combined that with just the long wavelength part of the SC as the Stokes, thus losing the energy in the short-wavelength part of the SC and reducing signal power [27, 36, 37]. We wanted to prevent the waste of that short-wavelength power so, motivated partly by the recently reported technique using intra-pulse frequency combinations for broadband-spectrum-based 'hyperspectral' 3-color CARS [13], we have used the full spectrum from an All Normal Dispersion (ANDi) fiber, NL-1050-NEG-1 from NKT Photonics, to produce a coherent continuum [38] and demonstrated its use for SF-CARS and SHG/SFG imaging. We have avoided what some people see as a drawback of 3-color CARS, which is that it requires a synchronous narrowband (few ps equivalent bandwidth) probe, which generally necessitates a complex laser system. A secondary point is that it has issues related to both to the poor polarization extinction ratio and to the fiber-length dependent de-coherence of the continuum [39], but those could probably be addressed in the future. We build on the understanding of the length dependent properties of the continuum from Ref. [40] (also partially discussed in [41]) and transferred the capability, used in Ref. [35], that incorporated an expensive pulse shaper to perform multimodal epi-imaging, but we use only glass blocks for matching the chirp of the pump and Stokes pulse, as in Ref. [28]. Hence we have reduced cost and complexity while still enabling high Raman resolution to be achieved throughout the CARS spectral ranges targeted. Critical to our work was the use of a MOF with precisely tailored length, chosen by a combination of experimental work and detailed numerical simulations instead of the approximate analytical approaches used in earlier work [24, 25]. We tailored the emission at the fiber output both in regard to the bandwidth and the linearity of the chirp when seeded by our standard 100 fs Ti:Sa laser. We then experimentally demonstrate the GDD equalization over the vibrational frequency range of 1000-3050 cm^{-1} with our opto-mechanical, modular, Variable GDD Equalizing Module (VGEM) which enabled the amount of glass in the path of the Stokes beam to be changed in a quasi-continuous, modular way. We image mouse adipose tissue, in a dual-channel setup, where the signal is separated into SHG/SFG and CARS/TPF detectors, enabling concurrent multimodal imaging. Note that SFG did not require pulse compression, so no post-processing of the SFG and CARS images was needed with respect to image registration: This is a clear advantage compared to systems that record the images from various modalities only after a delay while changing the pulse parameters of the laser and which thus require algorithms to post-process the data.

Our work presents a step forward in terms of providing higher power spectral density without compromising on the spectral resolution and wavenumber range which is a technological roadblock for previously used fibers such as femtoWHITE [31]. Moreover, the work presents spectral focusing imaging results without the use of a pulse shaper, yet achieves comparable results where such a device was used [42], thus making the setup simpler and inexpensive . Moreover, our work presents more efficient utilization of power output of the fiber unlike [42] wherein symmetric Stokes broadening is used and therefore inevitably leads to only partial utilization of the output. Overall, our approach provides several benefits in terms of performance at reduced complexity while at the same time it enables imaging of clinically relevant thick samples.

2. Materials and Methods

2.1 The requirement for GDD equalization in SF-CARS

In SF-CARS, the hyperspectral capability is achieved by changing the temporal overlap (practically achieved by changing the delay between the pump and the Stokes pulses). This is illustrated schematically in Fig. 1. However, unwanted but physically unavoidable, higher order dispersion influences the spectral resolution at different target instantaneous frequency differences (IFDs) (shown for IFDs: Ω_1, Ω_2 and Ω_3 in Fig. 1a-b). This means that the GDD needs to be equalized for each target resonance in turn for each image. The simulation data from our modelling shows that we have created a relatively narrow-band pump (ω_P) and a broadband Stokes (ω_S). The Instantaneous Frequency Differences (IFDs, Ω) are narrow or broad depending on the GDD equalization. For different target vibrational frequencies or IFDs different amounts of GDD compensation is required for optimal spectral resolution across all parts of the Stokes spectrum. The spectral width of the excitation is shown in the lower row. As illustrated in (a-i), with insufficient GDD equalization Raman peaks across the entire frequency range between Ω_2 and Ω_3 are being targeted; whereas in (a-ii) where GDD is more equal, a single resonance, Ω_1 is targeted. Similarily, in (b) if additional GDD equalization is applied to the low frequency part of the Stokes beam, then it is possible to achieve similar, good resolution for a vibrational frequency of Ω_2.

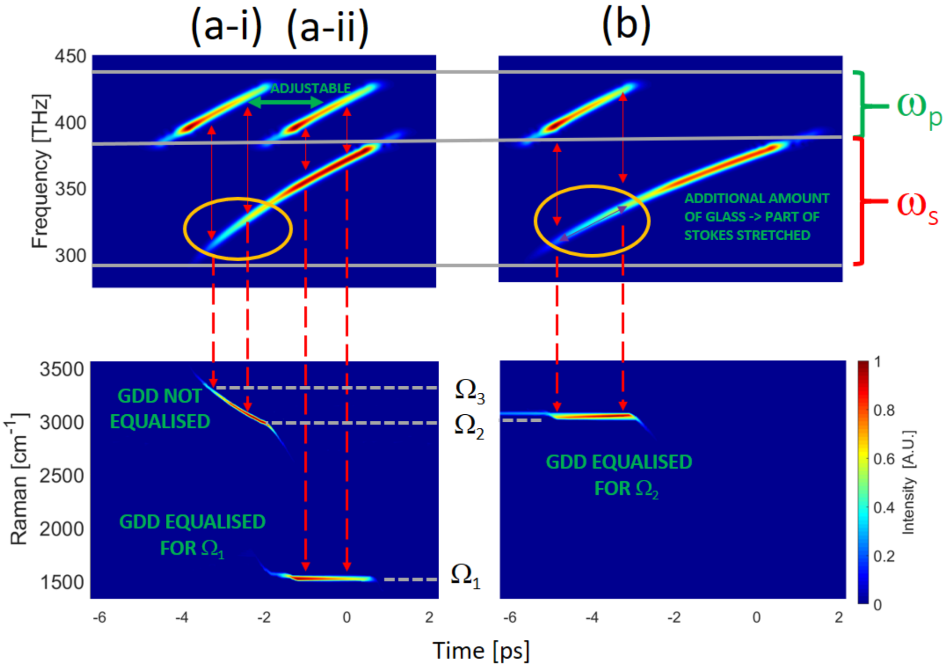

Figure 1. Spectrograms of the broadband optical pulses (top row) and resulting Raman band excitation frequencies (bottom row) showing the principle of SF-CARS. Top Row: Broadband stretched pulses separated into Pump and Stokes segments with a dichroic filter and shown with various relative delays applied. Bottom row: Frequency difference between the Pump and Stokes shown vs. arrival time. (a-i) vs. (a-ii) Broad range of excited frequencies, i.e. poor CARS resolution, shown for unequally chirped Pump vs. Stokes when using part of the spectrum that lies far from the cut-frequency. (b) Narrow excitation band using same spectral regions as (a-i) but after GDD equalization.

2.2 Simulations: theory and method

In SF-CARS, hyperspectral capabilities are dependent on the spectral width of the laser source. In the case of a non-linear fiber-based source the spectral width is dependent on a set of parameters, which need to be explored for optimization. Fiber-length optimization was done initially using numerical simulations and with the desired target pulse characteristics considering purely the CARS modality. Simulations based on the Generalized Non-Linear Schrödinger Equation (GNLSE) shown in Eq. (1) [33, 44] are solved using the code reported by our group previously in Ref. [44]. Here, the fiber loss is α, the second order dispersion is β_2 and γ is the nonlinearity parameter. The displacement of the pulse along the fiber length is z. The Raman and Brillouin effects have not been considered because of their negligible influence in a short piece of fiber. We used the experimental laser parameters i.e. central wavelength of 800 nm, pulse duration of 130 fs, and the conversion to peak power was based on an 80 MHz repetition rate with a maximum average power of 280 mW.

$$i\frac{\partial A}{\partial z}+\frac{i\alpha}{2}A-\frac{\beta_2}{2}\frac{\partial^2 A}{\partial T^2}+\gamma|A|^2A=0 \qquad (1)$$

2.3 Imaging setup, GDD equalization and image acquisition

A schematic of the spectral focusing CARS setup is presented in Fig. 2. The spectrum is divided into the pump and Stokes beams, as shown via our experimentally measured spectra (Fig. 2 inset). A MaiTai (Spectra Physics) laser was used as the source and was coupled into an ANDi fiber for the generation of a tailored broadband pulse for SF-CARS. The microstructured ANDi fiber was cut to the desired length using a fiber cleaver and each of the ends was sealed with a glass end-cap to inhibit degradation of the fiber. The laser light was coupled into the ANDi fiber with 50% efficiency, resulting in an output of 280 mW. We employed a metal pressure plate to compress the fiber in one direction to improve the polarization stability as suggested in Ref. [45]. This reduced the depolarization to less than 30% for 280 mW average power and thus enabled SF-CARS imaging of biological samples in the epi-direction with a high signal-to-noise ratio. An alternative would be to procure the polarization maintaining version of this fiber, but that was not available to us here.

The output beam was collimated using an achromatic lens (Thorlabs AC064-013-B-ML f=13 mm) and then divided into pump and Stokes components (inset Fig. 2) using a dichroic filter with a cut-off at 775 nm (Semrock FF775-DI01-25X36). The pump pulse was directed into a delay line (STANDA 8MT175-200), which provides displacement with a resolution of up to 310 nm which corresponds to a temporal displacement of 2 fs in the retro-reflection setup used here. The stage is equipped with an encoder providing feedback on its position and ensuring reproducibility of the temporal offset. The VGEM device was constructed simply by assembling anti-reflection coated polished glass blocks in a line. Up to 5 x 12 mm thick glass blocks (Thorlabs WG12012-B) blocks and 1 block of 5 mm thick glass (Thorlabs WG11050) were used in either a single- or double-pass arrangement to provide a total insertion length of up to 130 mm. Flip-mounts ensured that the path length through the VGEM was easy to adjust. The pump and Stokes beams were recombined using an identical Semrock FF775-DI01-25X36 dichroic and were aligned collinearly and coupled into an upright microscope (Leica DM305) through a pair of scanning galvanometric mirrors (Cambridge Technology 6220H). All optical components had an appropriate AR coating to reduce losses for the near infrared beams.

A 63x water immersion objective with NA=1.2 from Leica was used for the imaging and spectroscopy experiments. The objective lens is corrected for aberration in the visible and NIR (up to 1100 nm) which is important for multimodal imaging with different excitation wavelengths. The average power at the focal point was measured to be 16 mW for the pump (spectral width 70 nm), and 23 mW for the Stokes (spectral width 130 nm), which in total corresponds to an average PSD of >180 μW/nm. Images were acquired in the back-scattered geometry using non-descanned detection, since for multiphoton techniques there is no requirement to use a confocal pin-hole to reduce out-of-focus signal. Hamamatsu PMT detectors (H10722-01, H10722-20) were used for the simultaneous detection of CARS/TPF and SHG/SFG signals respectively. The signals were separated from the SC using a 694 nm short pass dichroic (Semrock FF02-694/SP-25) and further a 550 nm long pass filter (Thorlabs 550LP) and 400 nm bandpass filter (FB400-40) for the CARS and SHG/SFG imaging channels, respectively. ScanImage software (Vidrio Technologies) was used to acquire the images pixel-by-pixel [46]. All bio-images were acquired in a 1024 pixel x 1024 pixel format, with a dwell time of 32 μs per pixel. The images shown in Figure 8 were acquired without any averaging and hence are single-frame acquisitions while the images presented in Figure 9 are averages over 6 frames. All images were taken with 16 mW for the pump (spectral width 70 nm) and 23 mW for the Stokes (spectral width 130 nm) as stated above. The pure fluorescent background has been subtracted from pictures acquired in CARS modality.

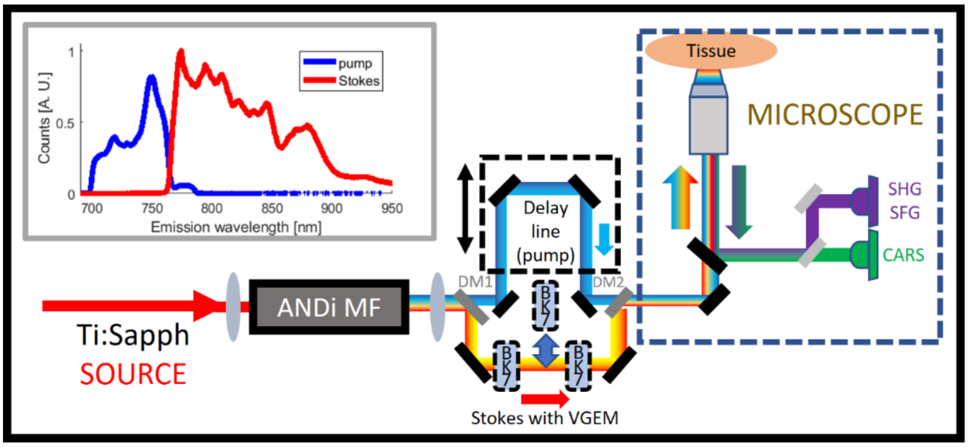

Figure 2. Schematic of the spectral focusing CARS setup. The ANDi-microstructured fiber (ANDi MF) is used for the generation of a broadband spectrum. A dichroic mirror, DM1, carves out the pump and Stokes beams (spectra shown inset). The delay line ensures temporal overlap at the sample. The modular Variable GDD Equalizing Module (VGEM) balances the GDD of the Stokes relative to the pump. Then, the collinear beams are coupled into the microscope for imaging and the back-scattered signal is collected, split for the different modalities and focused onto PMTs for non-descanned detection.

2.4 Sample preparation

For preliminary spectroscopy, solid dry samples of thymine (T0376, Sigma), deuterated palmitic acid (366897, Sigma) and 40 µm polystyrene (PS) beads (Fisher) were used for calibration. Each of these samples were prepared separately by placing a tiny amount (~0.1 mg) of each on a standard glass microscope slide under a coverslip (#1.5; 0.17 mm thick), the edges of which were sealed with a nitrocellulose-based varnish in order to allow imaging with a water immersion objective, as otherwise the water would leak inside and wash away the sample. Additionally, a sample containing a mixture of 40 µm polystyrene (PS) and polymethylmethacrylate (PMMA) beads was prepared in the same manner as above for the three single component samples.

Biological samples were prepared by excising tissues from culled mice. All procedures were carried out in accordance with the Animals (Scientific Procedures) Act 1986 set out by the UK Home Office. Female C57BL/6 mice aged between 4-6 months were culled via CO_2 and cervical dislocation. The adipose tissue was removed using scissors and a pair of forceps. The sample was finally washed in Phosphate Buffered Saline (PBS) immediately before being mounted on a microscope slide and sealed under a coverslip (#1.5; 0.17 mm thick) before imaging. All subsequent imaging was done without the addition of any stains/dyes and can be therefore qualified as label-free.

2.5 Acquisition of spontaneous Raman reference- and SF-CARS test-spectra

The spontaneous Raman spectra for thymine and deuterated palmitic acid, necessary for creating a calibrated reference to be subsequently compared with the CARS spectra, were acquired using a 633 nm laser, a 20x (0.8 NA) objective using a Renishaw 2000 micro-spectroscopy system set for 20 s acquisition times and averaged over 3 spectra. The spectrum for polystyrene was taken with a home-built Raman micro-spectrometer system utilizing a Shamrock303 spectrograph with an Andor iDus420 camera as the detector and equipped with a 785 nm laser. The spectrum was acquired with a single 20 second exposure with 0.6 mW laser power using a 40x (0.9 NA) objective.

For these non-biological samples, SF-CARS spectra (e.g. in sections 3.2-3.4, below) were recorded by acquiring images of the sample slides of each material separately using different relative delays between the pump and the Stokes beams and then plotting the image intensity for the specific region of interest with respect to the delay. These spectra were used only for calibration. Next, we used the sample which had the admixture of the different polymer beads to demonstrate chemically-selective contrast via hyper-spectral

SF-CARS. Images (in sections 3.4 and 4 below) were acquired with 128 pixel x 128 pixel resolution with 60 µs pixel dwell time following averaging over 3 recorded frames.

3. SF-CARS characterization: Results and discussion

While a key achievement here is the demonstration of multi-modal (CARS, SHG/SFG and TPF) imaging using a single seed laser, here we mainly consider and discuss our results in relation to the complex yet powerful method of SF-CARS. For all the data shown we have used the epi-detection geometry most suited to bio-imaging of thick samples.

3.1 Numerical simulations of SC generation, GDD equalization and SF-CARS generation efficiency

Simulation results for the ANDi fiber output spectra with an average power of 280 mW are presented in Fig. 3a. The spectral broadening is seen to be larger for longer lengths of the fiber. Furthermore, for longer fiber lengths, the central region of the spectrum becomes steadily broader and the wings of the pulse spectrum contain higher fractions of the total energy. However, further broadening beyond a length of approximately 9 cm of fiber was relatively minor.

To estimate our SF-CARS excitation efficiency, the power-spectral-density directly from the fiber output (P(λ)) was filtered spectrally in a numerical way to account for the transmittance (T_D) and the reflectance (R_D) of the dichroic beam splitters used in the delay line in our setup so as to estimate the expected experimental pump and Stokes spectra at the microscope focus. The anti-Stokes signal obtained upon targeting each instantaneous frequency difference was then integrated across the whole duration of pump-Stokes overlap (see Fig. 1). This last step required consideration of the temporal overlap of the pulses, so we used the output of the simulation (as described in section 2.1) and calculated the predicted GDD added by the glass blocks and other optical elements in the beam. We used Eq. (2-4) below, in which λ_1 and λ_2 are the wavelengths of the pump and Stokes beams needed for targeting a Raman resonance at frequency offset of Ω_1, B_A is the beam area of the focused laser at the sample, I_p and I_s are the intensities of the pump and Stokes beams respectively. The CARS signal is calculated for each of the components of the overlapped parts according to (4) taking into account the intensities only, and assuming a proportionality constant R=1.

$$I_S(\lambda) = \frac{P(\lambda_1)T_D^2}{B_A} \quad (2) \qquad I_p(\lambda) = \frac{P(\lambda_2)R_D^2}{B_A} \quad (3) \qquad I_{CARS}(\Omega_1) \sim R I_p^2(\lambda_1) I_S(\lambda_2) \quad (4)$$

The anti-Stokes output power was then filtered to account for the effects of the dichroic beam-splitters separating the signals to provide the estimated detected response for each Raman resonance targeted. The results vs fiber length are shown in Fig. 3(b). The power targeting high wavenumbers is lower for a 4 cm compared to a 9 cm length of fiber. However, increasing to 12 cm causes only minor additional power, so a length of 9 cm was selected for further study. We next considered the linearity of the slope of the frequency vs. time mapping at the fiber output as any distortion makes it more difficult to match pump and Stokes beams. The key factor is the so-called ‘wave-breaking length’, which determines the end of the first (and most rapid) stage of the spectral broadening, beyond which dispersion becomes dominant, leading to a subsequent predominance of temporal broadening [47]. Linearly chirped pulses are produced with 1x to 2x the wave-breaking length and as at the 280 mW power level, the wave-breaking length was ~5 cm, the 9 cm length is appropriate. (From a purely technical perspective, we found this length was convenient with standard fiber holders e.g. HFV002 from Thorlabs)

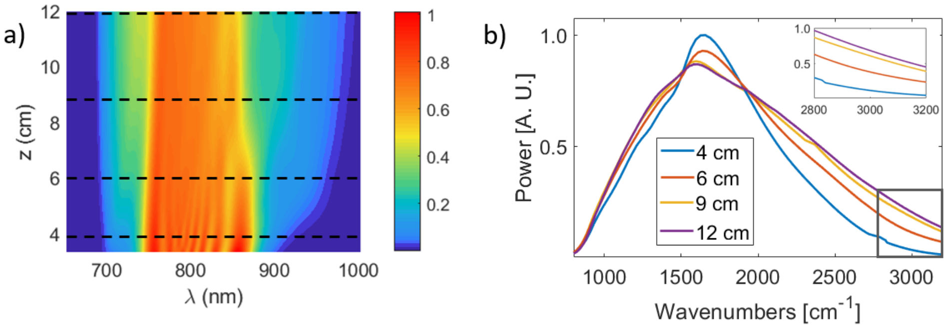

Figure 3. Simulation results: (a) Spectrum from the ANDi fiber vs. length; (b) CARS excitation power at the microscope focus for various fiber lengths. All data is for 280 mW of power at the fiber output. (Total pulse energy 3.5 nJ.)

We next plotted the predicted power dependence of both the numerical spectra and experimental spectra (Fig. 4). The spectra steadily broaden with power and there is good agreement between the simulations and measurements. The slight differences we observe may be attributed to the use of a scalar GNLSE rather than a vector-coupled model.

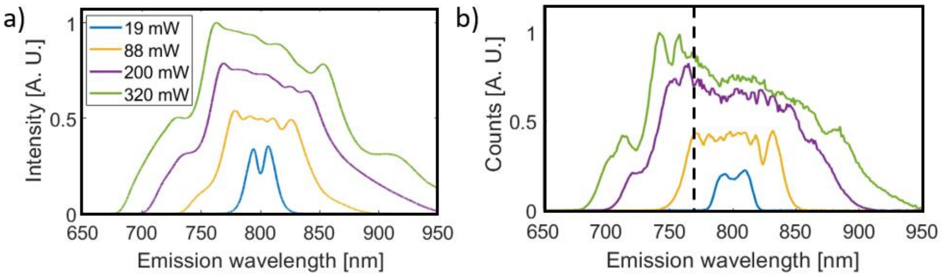

Figure 4. Output spectra from 9 cm ANDi fiber vs. output power. a) Simulation results; and b) Experimental data. The dashed line in b) indicates the separation between the pump and Stokes for SF-CARS.

3.2 Temporal characteristics of the continuum and GDD equalization

Calculations indicated that the durations of the chirped pump and Stokes before GDD equalization should be ~600 fs and 1.7 ps, respectively. (Direct temporal measurement of such broadband pulses would require a modified FROG, as reported in refs. [48, 49], so was beyond the capabilities available to us.) The GDD in both the pump and Stokes beam path needs to be equalized after transmission through all of the microscope optics [24]. We first used simulations to estimate the GDD equalization required between the pump and Stokes for each targeted Raman resonance, and then refined these estimates experimentally using our VGEM. For the simulations, we estimated the total thickness of the lenses and transmission filters after the fiber to be equivalent to 14 cm of BK7. For glasses most often used in microscopy optics, the GDD decreases at longer wavelengths (e.g. the dispersion zero for fused silica is close to ~1300 nm). Therefore the additional glass blocks were placed in the longer-wavelength Stokes beam. GDD equalization for each Raman resonance, that is the target instantaneous frequency difference (IFD), was calculated based on dispersion, as per data for N-BK7 glass [50]. Thus for targeting an IFD of 2800-3050 cm^{-1} the amount of additional GDD equalization was 72-125 mm, reducing to 60 mm for 2100 cm^{-1} IFD and 36 mm for 1678 cm^{-1} IFD. The 6 blocks of glass in the VGEM could be used in single or double pass, giving 12 - 130 mm of additional BK7 (as detailed in section 2.3 earlier).

The dependence of the achievable spectral resolution on the VGEM glass path is plotted in Fig. 5a)-b) by integrating over the entire temporal overlap between pump and Stokes. Figure 5a) shows that with a fixed length of BK7 in the Stokes path, the highest Raman resolutions are only achievable for a limited range of targeted IFDs. It is noted though that even when optimized, the spectral resolution is not uniform across the whole spectral range, predominantly due to residual higher order dispersion but also to a lesser extent due to the discrete increments in glass path (VGEM, in our case). Figs. 5b)(i-iii) show the profiles for the three cases: the fingerprint (900-1800 cm^{-1}), the so-called ‘silent’ (1800-2800 cm^{-1}) and the CH-stretching (2800-3200 cm^{-1}) regions confirming that the GDD compensation also maximises the anti-Stokes signal.

To check the predictions three chemicals with prominent Raman peaks in each of the above spectral regions were used, namely, thymine, deuterated palmitic acid and polystyrene respectively. Results for palmitic acid are shown in Fig. 5c). The measured peaks become higher and narrower with the addition of the appropriate amount of glass, whereas both under- and over-compensation result in lower resolution, confirming the trends in the simulations.

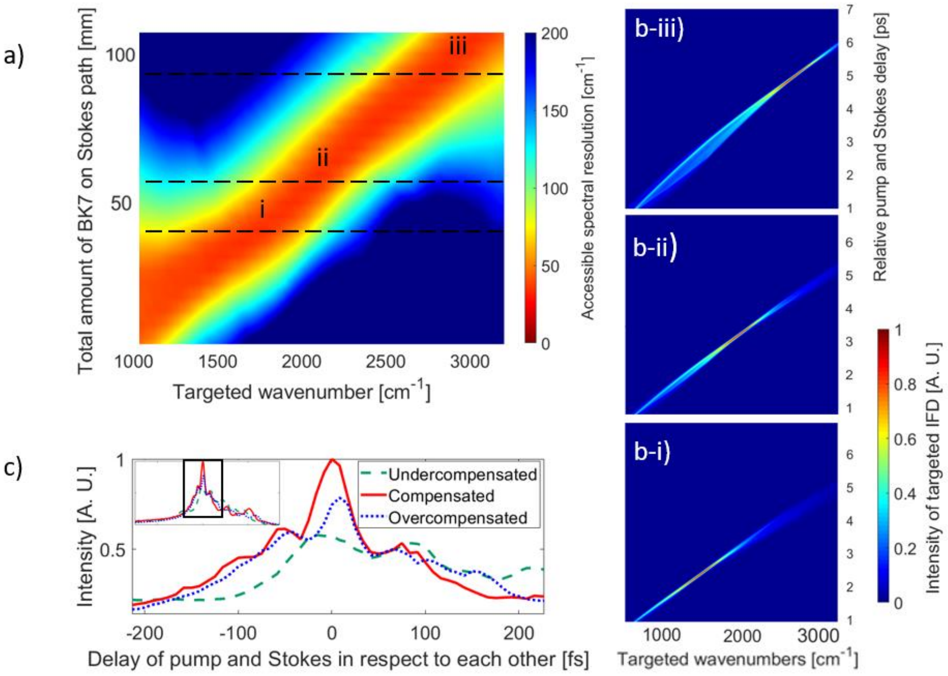

Figure 5. SF-CARS resolution vs. the length of BK7 glass added into the Stokes path. a) Calculated SF-CARS resolution (FWHM) as a function of Raman frequency and on BK7 added (from 0 to 120 mm). Dashed lines: i) 36 mm, ii) 60 mm and iii) 100 mm correspond to the BK7 insertion lengths used for the simulations shown in b) i-iii). b) Simulated anti-Stokes signal power vs. wavenumber for fixed amounts of BK7 in the VGEM. The BK7 lengths used were optimized for targeting the principal regions of interest: i) fingerprint region, ii) deuterated region and iii) CH region. c) Experimentally measured SF-CARS spectrum of deuterated palmitic acid with partial, full and excess GDD compensation. (Delay between pump and Stokes shown with respect to the position of the 2100 cm^{-1} peak. Better resolution and signal intensity are achieved with 60 mm of BK7 GDD compensation than with either 24 mm (under-), or 84 mm (over-compensation). The inset shows the anti-Stokes spectrum measured across a broader range.)

The SF-CARS spectra for thymine and polystyrene using the optimum VGEM glass thicknesses as well as measured spontaneous Raman spectra are shown in Fig. 6. The SF-CARS resolution was well matched to the widths of the peaks in the spontaneous data and we achieved 30 cm^{-1} (full-width half maximum) and 37 cm^{-1} for the 1372 cm^{-1} and 1678 cm^{-1} thymine peaks and 40 cm^{-1} for the 3054 cm^{-1} polystyrene peak. The resolutions achieved here agree well with the 36 cm^{-1} resolution predicted using the approximate analytic equation (Eq. (5)) from Ref. [25] calculated from the width of our measured pump/Stokes spectra and our calculated pulse durations. Hence the VGEM operated successfully across the entire Raman frequency range needed for bio-imaging. However, we note that the width of 1374 cm^{-1} peak is narrower than the 1678 cm^{-1} peak. We attribute the apparent improvement in resolution at lower wavenumbers to be due to filtering-out of a part of the emitted anti-Stokes wavelengths by our detection setup. We further note that the CH stretching bands for polystyrene at 2850 and 2930 cm^{-1} and the PMMA at 2957 cm^{-1} are inherently broad. Therefore, the spectral-focused CARS spectra are further broadened due to the dispersive nature of peaks.

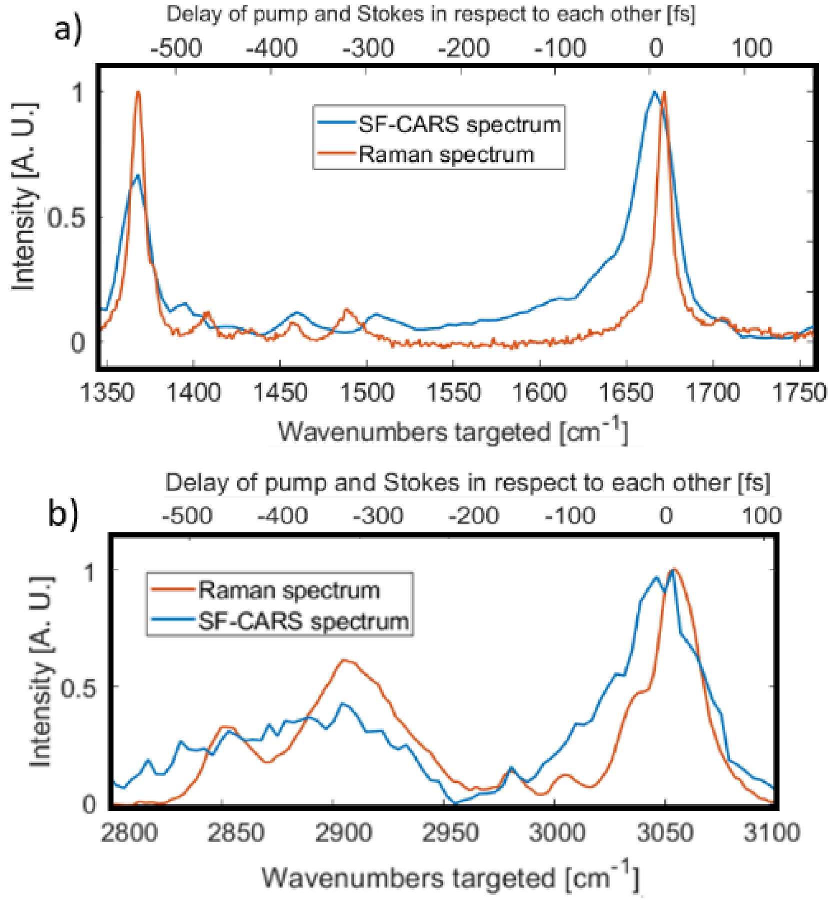

Figure 6. Experimental data showing the achievable resolution and the calibration of the relative pump vs. Stokes temporal delay (in fs) vs Raman resonance offset (in cm^{-1}). Spontaneous Raman spectra (red) and SF-CARS spectra with optimized GDD equalization (blue). a) thymine (finger-print region: VGEM pathlength 36 mm); and b) polystyrene (CH stretch region: VGEM pathlength 125 mm). The temporal delays are relative to the position targeting the a) 1672 cm^{-1} thymine peak and the b) 3050 cm^{-1} polystyrene peak in the respective graphs.

Given that SF-CARS allows access to finger-print and the high-frequency CH stretching region a 30 cm^{-1} spectral resolution is acceptable wherein imaging of the main biomolecule classes such as lipids, proteins and DNA is required. However, for differentiating sub-classes of biomolecules such as saturated and unsaturated lipids or secondary structure of proteins, a resolution of better than 10 cm^{-1} is desirable. Clearly, there is a trade-off between resolution and signal strength. The complexity of the setup and the application are obvious considerations as well. For example in order to achieve a resolution of 10 cm^{-1} in our setup would have required further stretching of pulses by 3 times. This would entail having an additional 28 cm in the system (common beam path; in pump and Stokes) with a further 24 cm in the Stokes beam to image the range (1000 to 3200 cm^{-1}) of IFDs targeted above. This would further require a longer delay line to be able to target the full range of IFDs (finger-print through to the CH-stretch region). More notably this would decrease the peak power that would decrease CARS (and SHG/TPF) signal strength and hence limit the type of sample that can be imaged by SF-CARS.

3.3 SF-CARS temporal delay vs. Raman wavenumber calibration

We also calibrated the temporal delay (IFD) vs. Raman frequency shift to allow spectroscopic Raman characterization of samples by measuring just the position of the delay stage from its encoder at which the hyper-spectral SF-CARS peaks align with the independently measured spontaneous Raman peaks. Spontaneous Raman spectra and the registered (i.e. calibrated) SF-CARS spectra for thymine and polystyrene are shown above in Figs. 6 a), b). Small differences in actual CARS peak positions are to be expected due to the dispersive line-shapes and mixing with the non-resonant background in CARS. While further data processing, e.g. using a Kramers-Kronig transform [51] could separate those effects, here we use the best fit to the two main peak positions from the raw data as an approximation to demonstrate hyperspectral SF-CARS imaging.

3.4 Tuning speed for hyperspectral imaging with ANDi-fiber based SF-CARS

Tuning to different vibrational peaks is performed by controlling the temporal delay between pump and Stokes with the motorized linear stage (delay line). We demonstrate the changes in resulting image contrast optimization and chemically specific imaging that this enabled via a sample containing an admixture of visually identical beads made of different chemicals with closely spaced resonances (both in the CH_2 stretching region), namely polystyrene (PS) and poly-methyl methacrylate (PMMA). These are indistinguishable using white-light imaging but are clearly segregated with SF-CARS as seen from the recorded SF-CARS signal vs. wavenumber in Fig. 7a) and the false-color image in Fig. 7b). (This demonstration is similar to the broadband CARS data in Ref. [52].)

The maximum tuning speed with our delay stage was 32 cm^{-1}/ms, which enables switching between the extremes of the 900-3200 cm^{-1} range within 72 ms. Depending on pixel count, this is likely to be much faster than the image acquisition time at any single frequency (up to 20 s), so is not normally a limitation. Even higher speeds are possible, e.g. more-complex, tailored, SF-CARS systems have achieved microsecond scanning, so the scan speed can be made comparable with the single-pixel dwell-time [53].

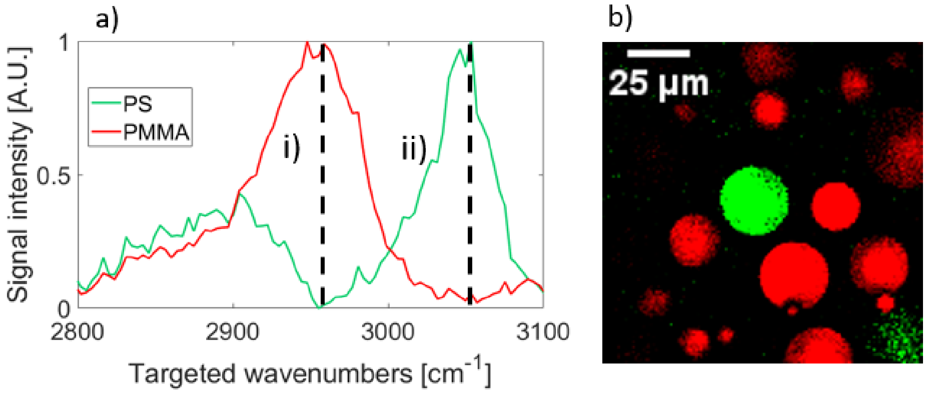

Figure 7. Hyperspectral imaging with our ANDi-fiber based SF-CARS setup. A sample containing a mixture of PS and PMMA beads was analysed. a) SF-CARS spectra after background subtraction corresponding to two different beads from the same sample are shown. The dashed lines correspond to the peak positions of i) 2957 cm^{-1} and ii) 3054 cm^{-1} associated with the two materials. The spectra were obtained by plotting the integrated intensity of the region of interest corresponding to two representative beads of each type. The intensities are normalised for each spectrum. b) shows the corresponding image with SF-CARS intensities at IFDs of 2957 cm^{-1} (red) and 3054 cm^{-1} (green) respectively which allows differentiation between the two types of beads. The brightness is indicative of the intensity of the signal at the respective IFDs. The image was acquired at an arbitrary depth and the beads are not monodisperse. Color intensity linearly relates to the counts on the detector, normalized to the maximum to obtain the highest contrast for each type of bead.

4. Multimodal bio-imaging imaging with ANDi-fiber source

We next demonstrate bio-imaging by showing CARS along with SHG/SFG and two-photon autofluorescence (TPaF) imaging in an epi-detection configuration. Image acquisition was carried out such that CARS and SGH/SFG images were simultaneously acquired first and then TPF simultaneously with SHG/SFG, on our two-channel detection setup. The SHG/SFG images, since they were common to the two successive acquisitions, allowed co-registration of the images from all 3 modalities. The pixel dwell times were the same for each of the modalities indicating similarity in signal levels. Each modality provides a different chemical or structural readout. We show representative images for adipose tissue from mice in Fig. 8. The parameters used during acquisition have been described in section 2.3. A schematic of the expected arrangement of different components in adipose tissue is shown in Fig. 8-i. It can be seen that the signal from the CH_2 stretching peak at 2845 cm^{-1} (Fig. 8-ii) is diffuse and not structurally dependent, as it is from uniform lipid distribution within the adipocyte (fat cell). Fig. 8-iii shows the corresponding SHG/SFG image. SHG is a special case of SFG and both interrogate the $\chi^{(2)}$ related part of the hyperpolarizability of materials. SFG is due to the mixing of two different wavelength photons while SHG is due to mixing of two photons of the same wavelength. Therefore, due to the broadband nature of our pump and Stokes beams we can get both SHG generated either by pump or Stokes (with signal quadratically proportional to the power of each) as well as SFG (caused because of the interaction of photons from pump and Stokes and hence proportional linearly to the power of each and also to their product). We verified through spectral measurements that indeed we observed both SHG and SFG at the same time. Since SHG and SFG both interact via the $\chi^{(2)}$ related part of the hyperpolarizability and so are generated only in non-centrosymmetric molecules or structures with order so that the boundaries lead to symmetry breaking. Here, SHG/SFG have been used to selectively image collagen fibers, which are a dominant component of adipose tissue scaffolding [54], highlighting the fibrillary nature and periodicity of collagen fibers in the sample. On the other hand, we used TPF to image autofluorophores in the tissue that had an emission in the range of 520+/-20 nm which has been attributed mainly to Flavin Adenine Dinucleotide (FAD) and Flavin Mononucleotide (FMN) [55]. These molecules indicate metabolic activity in cells. Thus the two-photon autofluorescence (TPaF) images (Fig. 8-iv), Adipose Tissue Macrophages (ATMs), that are metabolically active and localize in between adipocyte cells in such tissue. We verified that the TPaF signal was not delay dependent, and as such is not a four-wave mixing signal. Shape and distribution of the macrophages is similar to that observed by others [55], and our detection window covers the expected emission spectral range [56]. Fig. 8-iv and 8-v compare an optical (brightfield) image and the composite multimodal image of the same area of the tissue. While the brightfield image (acquired in transmission) gives only bulk morphological features the multimodal image gives the underlying chemical and structural distribution and the local adipose tissue architecture [55] through combined CARS, SHG and TPF modalities. An SF-CARS spectrum is shown in Fig. 8-vii corresponding to the lipid area shown in Fig. 8-ii which shows the characteristic CH_2 peak at 2845 cm^{-1}. While this confirms the selectivity of the CARS signals (in Fig. 8-ii) the ability to acquire spectroscopic information confers a unique advantage to SF-CARS for imaging samples of unknown compositions.

Currently tissue diagnostics makes use of colored stains on thin tissue slices (typically 5-7 µm in thickness) imaged in a transmission configuration, and hence samples require careful preparation and sectioning. Hence, for such diagnostic applications using label-free imaging on clinically relevant thick tissue samples (fresh from surgery, for example) in the

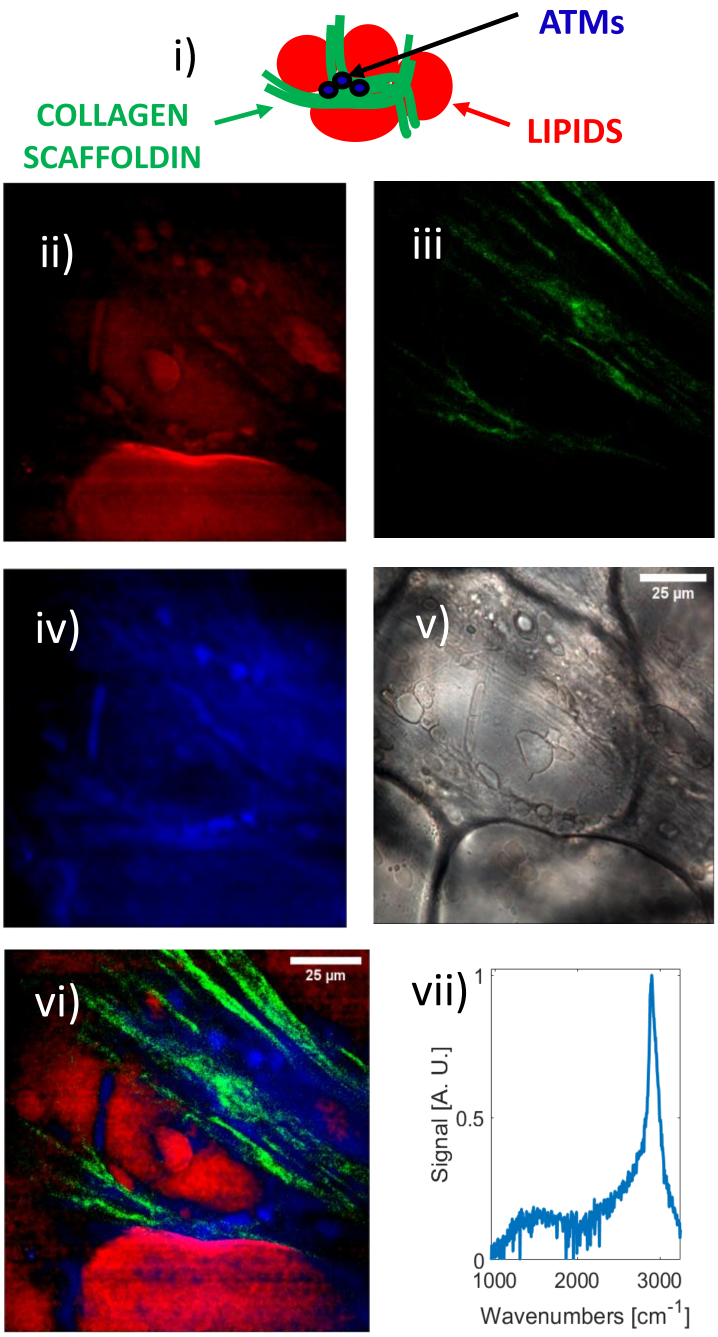

Fig. 8 Multimodal SF-CARS / SFG (SHG) / TPaF bioimaging with ANDi-fiber source. Images are of mouse adipose tissue acquired at the surface of the sample. i) Schematic showing the main components of adipose tissue; ii) CARS image mapping the intensity of the 2845 cm^{-1} lipid band across the tissue; iii) collagen fibers imaged with SHG/SFG; iv) TPEaF images FAD in macrophage cells; v) Bright field transmission image of the tissue, by its nature it is integrated over all the illuminated volume. vi) SF-CARS spectrum corresponding to the lipid area in adipose tissue; vii) Composite image with CARS, SHG and TPF overlaid. Color intensity linearly relates to the counts on the detector, normalized to the maximum to obtain the highest contrast for each of the channels independently. The images shown are single frame SF-CARS acquisitions with pixel dwell time of 32 µs, 16 mW pump and 23 mW of Stokes.

epi-detection would be preferable and present a significant advantage. Here we are able to show that with our fiber-enabled multimodal CARS imaging setup we can image at different depths in a thick (>25 µm) tissue sample (Fig. 9). The ability to image in 3D is preferable since tissue is intrinsically three-dimensional and sectioning can miss crucial information. However as expected the signals are weaker at depth compared to that on the surface. Here we were further constrained by the maximum power output from the fiber (and hence at the sample). The depth of focus is expected to be different for CARS (3-photon process) and SHG/TPF (2-photon processes); however, with the 1 µm z-resolution of our microscope stage we did not observe any significant effect. Overall, the simultaneous acquisition of the signals with the ANDi-fiber based SF-CARS setup shows CARS as well as multimodal imaging capability on thick tissue samples. The epi-detection capability with a fiber-based setup demonstrates the relevance to biological and clinical samples without the need for extensive sample preparation.

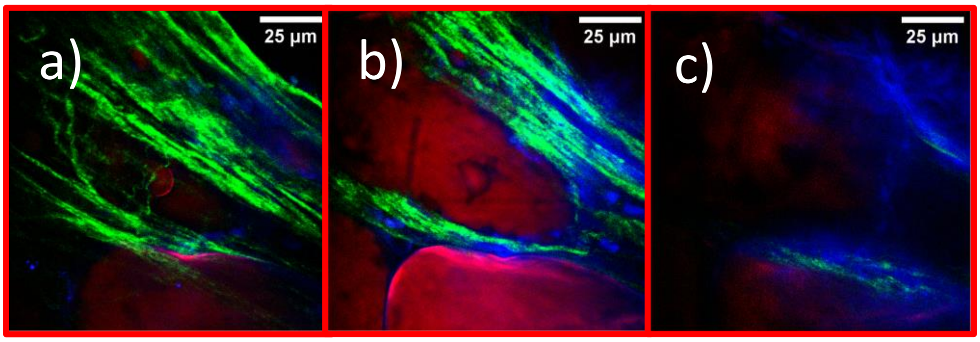

Fig. 9 Multimodal imaging at different depths. Composite images with the combined modalities of CARS (red), SHG/SFG (green) and TPaF (blue) corresponding to the image shown in Fig. 8-vi) are shown at different depths a) 0 µm , b) 10 µm and c) 18 µm. The depths refer to the distance into the tissue from the sample surface.

5. Summary and conclusions

In summary, we show for the first time that a length-optimized ANDi microstructured fiber can be used (retrofitted) with the typical workhorse, 100 fs Ti:Sa seed laser from multiphoton fluorescence imaging setups, to realize a simple yet powerful source for spectral-focusing CARS and concurrent SHG/SFG and two-photon fluorescence microscopy in an epi-detection geometry. Rapid and accurate tuning between resonances was achieved by changing the relative delay of pump and Stokes pulses via a motorized high-precision linear stage. Minor challenges remain such as polarization noise documented in Ref. [57], but a polarization-maintaining version of the fiber could be used in the future, subject to availability from the manufacturer. Numerical simulations of the interaction between pump and Stokes showed clearly the influence of the dispersion from the optics on the nonlinear chirp of the pump and Stokes hence providing crucial guidance on the length of glass to be used for GDD equalization in the Stokes beam. The resulting spectral resolution achieved was ~30-40 cm^{-1}, which is close to the maximum achievable considering the spectrum used and stretching of pulses. The continuum was generated from a 9 cm length of fiber and imaging was achieved at Raman frequencies between 900 and 3200 cm^{-1}, i.e. spanning the fingerprint region and the CH-stretching region, both of which are critical for bio-samples.

In conclusion, by combining elements of multiphoton techniques in a novel configuration, our work paves the way for the simple implementation of SF-CARS and concurrent SHG/SFG/TPF imaging. In other words, this work applied different technical solutions from the field of CARS and SF-CARS, and achieve maximal necessary spectral range and spectral resolution and dwell times comparable with previous papers, while utilizing much simpler setup. This stepping stone points to a lower cost future route to translation of nonlinear laser microscopy imaging via label-free CARS imaging for use on clinical samples in both medical diagnostics and bio-imaging research laboratories.

Funding

This work was supported by funding from the Institute for Life Sciences and the Optoelectronics Research Centre, University of Southampton, UK; ERC grant Nano-ChemBioVision (638258) and EPSRC grants EP/R041814/1, EP/P027644/1, EP/P012248/1 and also funding from Air Force Office of Scientific Research (AFOSR) (FA9550-14-1-0382).

References

1. Maker, P.D. and R.W. Terhune, *Study of Optical Effects Due to an Induced Polarization Third Order in the Electric Field Strength.* Physical Review, 1965. **137**(3A): p. A801-A818.
2. Duncan, M.D., J. Reintjes, and T.J. Manuccia, *Scanning coherent anti-Stokes Raman microscope.* Optics Letters, 1982. **7**(8): p. 350-352.
3. Zumbusch, A., G.R. Holtom, and X.S. Xie, *Three-Dimensional Vibrational Imaging by Coherent Anti-Stokes Raman Scattering.* Physical Review Letters, 1999. **82**(20): p. 4142-4145.
4. Müller, M. and A. Zumbusch, *Coherent anti‐Stokes Raman Scattering Microscopy.* ChemPhysChem, 2007. **8**(15): p. 2156-2170.
5. Evans, C.L. and X.S. Xie, *Coherent Anti-Stokes Raman Scattering Microscopy: Chemical Imaging for Biology and Medicine.* Annual Review of Analytical Chemistry, 2008. **1**(1): p. 883-909.
6. Bélanger, E., et al., *In vivo evaluation of demyelination and remyelination in a nerve crush injury model.* Biomedical Optics Express, 2011. **2**(9): p. 2698-2708.
7. Le, T.T., T.B. Huff, and J.-X. Cheng, *Coherent anti-Stokes Raman scattering imaging of lipids in cancer metastasis.* BMC Cancer, 2009. **9**: p. 42-42.
8. Konorov, S.O., et al., *In Situ Analysis of Living Embryonic Stem Cells by Coherent Anti-Stokes Raman Microscopy.* Analytical Chemistry, 2007. **79**(18): p. 7221-7225.
9. Smus, J.P., et al., *Tracking adipogenic differentiation of skeletal stem cells by label-free chemically selective imaging.* Chemical Science, 2015(6): p. 7089-7096.
10. Evans, C.L., et al., *Chemical imaging of tissue in vivo with video-rate coherent anti-Stokes Raman scattering microscopy.* Proceedings of the National Academy of Sciences of the United States of America, 2005. **102**(46): p. 16807.
11. Jung, Y., et al., *Longitudinal, 3D In Vivo Imaging of Sebaceous Glands by Coherent Anti-Stokes Raman Scattering Microscopy: Normal Function and Response to Cryotherapy.* Journal of Investigative Dermatology, 2015. **135**(1): p. 39-44.
12. Camp Jr, C.H. and M.T. Cicerone, *Chemically sensitive bioimaging with coherent Raman scattering.* Nature Photonics, 2015. **9**: p. 295.
13. Camp JrCharles, H., et al., *High-speed coherent Raman fingerprint imaging of biological tissues.* Nat Photon, 2014. **8**(8): p. 627-634.
14. Steuwe, C., et al., *Surface Enhanced Coherent Anti-Stokes Raman Scattering on Nanostructured Gold Surfaces.* Nano Letters, 2011. **11**(12): p. 5339-5343.
15. Lee, Y.J., Y. Liu, and M.T. Cicerone, *Characterization of three-color CARS in a two-pulse broadband CARS spectrum.* Optics Letters, 2007. **32**(22): p. 3370-3372.
16. Monfort, T.R., *Non linear photonics: developments & applications in biomedical imaging, PhD Thesis*. 2018, University of Southampton.
17. Rocha-Mendoza, I., W. Langbein, and P. Borri, *Coherent anti-Stokes Raman microspectroscopy using spectral focusing with glass dispersion.* Applied Physics Letters, 2008. **93**(20): p. 201103.
18. Zipfel, W.R., R.M. Williams, and W.W. Webb, *Nonlinear magic: multiphoton microscopy in the biosciences.* Nat Biotech, 2003. **21**(11): p. 1369-1377.
19. Chen, X., et al., *Second harmonic generation microscopy for quantitative analysis of collagen fibrillar structure.* Nature protocols, 2012. **7**(4): p. 654-669.
20. Cheng, J.-x., et al., *An Epi-Detected Coherent Anti-Stokes Raman Scattering (E-CARS) Microscope with High Spectral Resolution and High Sensitivity.* The Journal of Physical Chemistry B, 2001. **105**(7): p. 1277-1280.
21. Volkmer, A., J.-X. Cheng, and X. Sunney Xie, *Vibrational Imaging with High Sensitivity via Epidetected Coherent Anti-Stokes Raman Scattering Microscopy.* Physical Review Letters, 2001. **87**(2): p. 023901.
22. Hellerer, T., A.M.K. Enejder, and A. Zumbusch, *Spectral focusing: High spectral resolution spectroscopy with broad-bandwidth laser pulses.* Applied Physics Letters, 2004. **85**(1): p. 25-27.
23. Cheng, J.-X. and X.S. Xie, *Coherent Anti-Stokes Raman Scattering Microscopy: Instrumentation, Theory, and Applications.* The Journal of Physical Chemistry B, 2004. **108**(3): p. 827-840.
24. Cole, R.A. and A.D. Slepkov, *Interplay of pulse bandwidth and spectral resolution in spectral-focusing CARS microscopy.* Journal of the Optical Society of America B, 2018. **35**(4): p. 842-850.
25. Mohseni, M., C. Polzer, and T. Hellerer, *Resolution of spectral focusing in coherent Raman imaging.* Optics Express, 2018. **26**(8): p. 10230-10241.
26. Langbein, W., I. Rocha-Mendoza, and P. Borri, *Coherent anti-Stokes Raman micro-spectroscopy using spectral focusing: theory and experiment.* Journal of Raman Spectroscopy, 2009. **40**(7): p. 800-808.

27. Porquez, J.G., et al., *Spectrally-broad coherent anti-Stokes Raman scattering hyper-microscopy utilizing a Stokes supercontinuum pumped at 800 nm.* Biomedical Optics Express, 2016. **7**(10): p. 4335-4345.
28. Pope, I., et al., *Simultaneous hyperspectral differential-CARS, TPF and SHG microscopy with a single 5 fs Ti:Sa laser.* Optics Express, 2013. **21**(6): p. 7096-7106.
29. Brückner, L., T. Buckup, and M. Motzkus, *Enhancement of coherent anti-Stokes Raman signal via tailored probing in spectral focusing.* Optics Letters, 2015. **40**(22): p. 5204-5207.
30. Porquez, J.G., R.A. Cole, and A.D. Slepkov, *Comparison of two photonic crystal fibers for supercontinuum-Stokes spectral-focusing-CARS hyperspectroscopy.* OSA Continuum, 2018. **1**(4): p. 1385-1399.
31. Pegoraro, A.F., et al., *Optimally chirped multimodal CARS microscopy based on a single Ti:sapphire oscillator.* Optics Express, 2009. **17**(4): p. 2984-2996.
32. Liu, Y., et al., *Broadband nonlinear vibrational spectroscopy by shaping a coherent fiber supercontinuum.* Optics Express, 2013. **21**(7): p. 8269-8275.
33. Dudley, J.M., G. Genty, and S. Coen, *Supercontinuum generation in photonic crystal fiber.* Reviews of Modern Physics, 2006. **78**(4): p. 1135.
34. Hilligsøe, K.M., et al., *Supercontinuum generation in a photonic crystal fiber with two zero dispersion wavelengths.* Optics Express, 2004. **12**(6): p. 1045-1054.
35. Tu, H., et al., *Stain-free histopathology by programmable supercontinuum pulses.* Nature Photonics, 2016. **10**: p. 534.
36. Porquez, J.G., et al., *Brighter CARS hypermicroscopy via spectral surfing of a Stokes supercontinuum.* Optics Letters, 2017. **42**(12): p. 2255-2258.
37. Li, B., P. Borri, and W. Langbein, *Dual/differential coherent anti-Stokes Raman scattering module for multiphoton microscopes with a femtosecond Ti:sapphire oscillator*. Vol. 18. 2013: SPIE. 1-6, 6.
38. Heidt, A.M., et al., *Limits of coherent supercontinuum generation in normal dispersion fibers.* Journal of the Optical Society of America B, 2017. **34**(4): p. 764-775.
39. Lee, Y.J., et al., *Optimized continuum from a photonic crystal fiber for broadband time-resolved coherent anti-Stokes Raman scattering.* Optics Express, 2010. **18**(5): p. 4371-4379.
40. Hooper, L.E., et al., *Coherent supercontinuum generation in photonic crystal fiber with all-normal group velocity dispersion.* Optics Express, 2011. **19**(6): p. 4902-4907.
41. Li, K.-C., et al., *Simple approach to three-color two-photon microscopy by a fiber-optic wavelength convertor.* Biomedical Optics Express, 2016. **7**(11): p. 4803-4815.
42. Pegoraro, A.F., et al., *Single laser source for multimodal coherent anti-Stokes Raman scattering microscopy.* Applied Optics, 2010. **49**(25): p. F10-F17.
43. Chen, K., et al., *Quantitative chemical imaging with background-free multiplex coherent anti-Stokes Raman scattering by dual-soliton Stokes pulses.* Biomedical Optics Express, 2016. **7**(10): p. 3927-3939.
44. Poletti, F. and P. Horak, *Description of ultrashort pulse propagation in multimode optical fibers.* Journal of the Optical Society of America B, 2008. **25**(10): p. 1645-1654.
45. Tu, H., et al., *Nonlinear polarization dynamics in a weakly birefringent all-normal dispersion photonic crystal fiber: toward a practical coherent fiber supercontinuum laser.* Optics Express, 2012. **20**(2): p. 1113-1128.
46. Pologruto, T.A., B.L. Sabatini, and K. Svoboda, *ScanImage: Flexible software for operating laser scanning microscopes.* BioMedical Engineering OnLine, 2003. **2**: p. 13-13.
47. Finot, C., et al., *Beneficial impact of wave-breaking for coherent continuum formation in normally dispersive nonlinear fibers.* Journal of the Optical Society of America B, 2008. **25**(11): p. 1938-1948.
48. Ellis, A. and U. Österberg, *RotaryFROG: geometry for measuring amplitude and phase of weak broadband laser pulses.* Optics Letters, 2009. **34**(4): p. 404-406.
49. O'Shea, P., et al., *Increased-bandwidth in ultrashort-pulse measurement using an angle-dithered nonlinear-optical crystal.* Optics Express, 2000. **7**(10): p. 342-349.
50. Schott North America, I. *Optical Glass Data Sheets*. 2014 [cited 2018; Available from: https://www.schott.com/advanced_optics/us/abbe_datasheets/schott-datasheet-all-us.pdf.
51. Liu, Y., Y.J. Lee, and M.T. Cicerone, *Broadband CARS spectral phase retrieval using a time-domain Kramers–Kronig transform.* Optics Letters, 2009. **34**(9): p. 1363-1365.
52. Lee, Y.J., et al., *Quantitative Image Analysis of Broadband CARS Hyperspectral Images of Polymer Blends.* Analytical Chemistry, 2011. **83**(7): p. 2733-2739.
53. Liao, C.-S., et al., *Stimulated Raman spectroscopic imaging by microsecond delay-line tuning.* Optica, 2016. **3**(12): p. 1377-1380.
54. Khan, T., et al., *Metabolic Dysregulation and Adipose Tissue Fibrosis: Role of Collagen VI.* Molecular and Cellular Biology, 2009. **29**(6): p. 1575.
55. Urasaki, Y., et al., *Imaging Immune and Metabolic Cells of Visceral Adipose Tissues with Multimodal Nonlinear Optical Microscopy*. PLOS ONE, 2012. **7**(6): p. e38418.
56. Huang, S., A.A. Heikal, and W.W. Webb, *Two-photon fluorescence spectroscopy and microscopy of NAD(P)H and flavoprotein.* Biophysical journal, 2002. **82**(5): p. 2811-2825.
57. Liu, Y., et al., *Suppressing Short-Term Polarization Noise and Related Spectral Decoherence in All-Normal Dispersion Fiber Supercontinuum Generation.* Journal of Lightwave Technology, 2015. **33**(9): p. 1814-1820.